Journal of Flow Control, Measurement & Visualization, 2022, 10, 117-147
https://www.scirp.org/journal/jfcmv
ISSN Online: 2329-3330
ISSN Print: 2329-3322

A Review of the Recent PIV Studies

—From the Basics to the Hybridization with CFD

Fujio Yamamoto[1], Masaaki Ishikawa[2]

[1]Graduate School of Engineering, University of Fukui, Fukui-Shi, Japan
[2]Energy and Environment Engineering Program, Faculty of Engineering, University of the Ryukyus, Okinawa, Japan
Email: yamamo96@yahoo.co.jp

How to cite this paper: Yamamoto, F. and Ishikawa, M. (2022) A Review of the Recent PIV Studies. *Journal of Flow Control, Measurement & Visualization*, **10**, 117-147.
https://doi.org/10.4236/jfcmv.2022.104008

Received: April 2, 2022
Accepted: July 25, 2022
Published: October 24, 2022

Abstract

The purpose of this article is to review recent PIV Studies from the basic to hybrid analysis, focusing on explaining epoch-making development of PIV. The overwhelming advantage of PIV over other velocity measurement methods is that it enables instantaneous and simultaneous velocity measurement of whole flow fields. We roughly classify PIV development and/or progress into the following five categories; A) Basics of PIV and post-processing. B) Simultaneous measurement of velocity and temperature, and 3D-PIV. C) Application to multiphase turbulent flows. D) Application to fluid machinery. E) Hybridization of PIV and CFD. This paper introduces the epoch-making research results from papers published in international journals as milestones related to (A) to (E), and concludes with additional forecast of future development of PIV research.

Keywords

Review, PIV, PTV, CFD, Hybrid, Fluid Mechanics, Measurement, Flow Visualization

1. Introduction

Research articles on PIV (Particle Image Velocimetry) and PTV (Particle Tracking Velocimetry) began to appear in academic journals in the first half of 1980. For 40 years since then, experimental fluid mechanics has undergone a revolutionary development with PIV. The reason is that PIV and PTV have the feature of enabling instantaneous and simultaneous velocity measurement of whole 2D and 3D flow fields. That is, their characteristics cannot be realized by the conventional Pitot-Tube or hot wire anemometer, or LDV, which is a flow velocity measurement method at one point and/or several points.

Adrian, R. J. (1991) [1] described the basic of conventional PIV, and this article is very useful for successive pioneering studies. Adrian, R. J. (2005) [2] also described not only the PIV fundamentals but also the research history and future prospects under the title of "*Twenty years of particle image velocimetry*" from the birth of PIV to 2004. Adrian, R. J. and Westerweel, J. (2011) [3] and also Raffel, M. *et al.* (2018) [4] published books entitled "*Particle Image Velocimetry*", and "*Particle Image Velocimetry—A Practical Guide*, 3rd *Ed.*", respectively, explaining the latest methods of PIV and introducing application examples. These article and books are useful and recommendable for researchers and engineers, who want to learn the basics and applications of PIV.

To avoid duplication with their works, the present article introduces the results of research that have played the important roles of new milestones since around 2000. In addition, in order to review the historical background, earlier articles referring to conventional PIV in time series are also introduced and evaluated. We try to classify the research papers into the following five categories. However, if one research article contributed to multiple categories, we will introduce such an article in the category with the highest contribution.

A) Basics of PIV and post-processing

B) Simultaneous measurement of velocity and temperature, and 3-D PIV

C) Application to multiphase turbulent flows

D) Application to fluid machinery

E) Hybridization of PIV and CFD

2. Basic Principle and Remarks of Conventional PIV and PTV

The algorithm of particle brightness-distribution pattern tracking is the most popular. Correct pairs of elements of particle clouds are obtained in two consecutive frames based on the similarity of image brightness distribution patterns between the two frames by calculating the values of the coefficient $C_{1,fg}$ or $C_{2,fg}$ of cross-correlation defined by Equation (1) or Equation (2):

$$C_{1,fg} = \frac{\sum_{i=0}^{N}\sum_{j=0}^{M} f_{ij} g_{ij}}{\sqrt{\sum_{i=0}^{N}\sum_{j=0}^{M} f_{ij}^2 \cdot \sum_{i=0}^{N}\sum_{j=0}^{M} g_{ij}^2}}, \tag{1}$$

$$C_{2,fg} = \frac{\sum_{i=0}^{N}\sum_{j=0}^{M} \left(f_{ij} - \bar{f}\right)\left(g_{ij} - \bar{g}\right)}{\sqrt{\sum_{i=0}^{N}\sum_{j=0}^{M} \left(f_{ij} - \bar{f}\right)^2 \cdot \sum_{i=0}^{N}\sum_{j=0}^{M} \left(g_{ij} - \bar{g}\right)^2}}. \tag{2}$$

Equation (1) is used for evaluating the similarity of functions of f for the first frame and g for the second frame, and Equation (2) for evaluating the similarity of dispersion of $\left(f - \bar{f}\right)^2$ and $\left(g - \bar{g}\right)^2$, and $\bar{f}$ and $\bar{g}$ are mean values of brightness.

The similarity of image brightness distribution patterns can also be evaluated by the method of minimum quadratic difference D_{fg} defined by Equation (3) or

by the method of summation of brightness difference E_{fg} defined by Equation (4):

$$D_{fg} = \frac{1}{NM}\sum_{i=0}^{N}\sum_{j=0}^{M}\left(f_{ij} - g_{ij}\right)^2, \tag{3}$$

$$E_{fg} = \sum_{i=0}^{N}\sum_{j=0}^{M}\left|f_{ij} - g_{ij}\right|. \tag{4}$$

In these equations, f_{ij} and g_{ij} are digital gray values of the pixels in the overlapped interrogation windows of size $M \times N$ pixels which consist of element of particle clouds in the two consecutive frames, When the maximum value of $C_{1,fg}$, $C_{2,fg}$, or the minimum value of D_{fg} or E_{fg} is found for a pair of the two interrogation windows, the pair is considered to be identified. The velocity of the particle clouds is computed as $\vec{v} = \vec{D}_{PQ}/\Delta t$ by using the displacement $\vec{D}_{PQ}$ of the two centers P and Q at the time interval Δt between the two frames.

Another type of techniques employs the algorithm of particle distribution pattern tracking, that is called PTV. Each particle motion is tracked and the particle velocity is calculated from the displacement of the particle center between two consecutive frames. One of the methods is called the binary image cross-correlation method (BICC), which uses binarized images of two consecutive frames for a high-speed calculation. The computation of the value of cross-correlation given by Equation (1) can be simplified as the following equation after a rigorous mathematical discussion described in Ref. [7]:

$$C_{5,fg} = \frac{L}{\sqrt{nm}}, \tag{5}$$

where L is the summation of logical products of the image brightness binarized with the value of 1 or 0 at each pixel in two overlapped interrogation windows for two consecutive frames, m and n are numbers of bright pixels in the first and second windows, respectively. The computational time of Equation (5) is much shorter than those from Equations (1) to (4). Therefore, the method of BICC can achieve a real time measurement of flow velocity fields. Besides, there are so-called the Delaunay tessellation technique and the velocity gradient tensor technique which also use two consecutive binarized images and high-speed performance to analyze not only translation but also the general fluid deformation such as rotation, shearing, expansion and compression as described in detail later. Those methods are, however, limited to the case of low number density of particles. Comparison of methods for conventional PIV and PTV are summarized in **Table 1**, whereas some recent key PIV studies will be introduced in each category of Chapter 3.

3. Five Categories of PIV and PTV

In the present article we classify PIV development and progress into the five categories as described in Section 3.1 to 3.5.

Table 1. Comparison of methods for conventional PIV and PTV.

Methods	Image Density	Number of frames	Dimensions	principles	Remarks
Direct cross-correlation method (Adrian, R. J. (1991) [1])	High	2	2	Maximum value of cross-correlation coefficient	Widely used in all the PIV, heavy computation
Minimum quadratic difference (Gui, L. C. and Merzkirch, W. (1996) [5])	High	1, 2	2	Minimum quadratic difference	Fair computation, good tracking property
Absolute gray level difference (Kaga, A., Inoue, Y. and Yamaguchi, K. (1994) [6])	High	2	2	Minimum summation of absolute value of brightness difference	Fast computation, fair tracking property
Auto-correlation method (Adrian, R. J. (1991) [1])	High	1	1	Maximum value of cross-correlation coefficient	Direction ambiguity
BICC (Yamamoto, F., Wada, A., Iguchi, M. and Ishikawa, M. (1996) [7])	Medium, Low	2, 3	2, 3	Maximum value of binary image cross-correlation	Widely used, good tracking, fast computation, the occurrence of some erroneous vectors
DT-PTV (Song, X., Yamamoto, F., Iguchi, M. and Murai, Y. (1999) [8])	Medium, Low	2	2, 3	Pattern tracked by Delaunay Triangles	Good tracking, fast computation, removing erroneous vectors automatically, fit for rotational flow, easier rearrangement
VGT (Ishikawa, M. *et al.* (2000) [9])	Medium, Low	2	2, 3	Pattern tracked by velocity tensor	Good tracking, fast computation, fit for rotational and shear flow, the occurrence of some erroneous vectors
Spring model (Okamoto, K., Hassan, Y. A. and Schmidl, W. D. (1995) [10])	Medium, Low	2	2, 3	Pattern tracked by constructed spring net	Good tracking, fast computation, fit for rotational and shear flow, the occurrence of some erroneous vectors
4-frame PTV (Nishino, K., Kasagi, N. and Hirata, M. (1989) [11])	Low	4	2, 3	Particles move along smooth curves	Fair tracking heavy computation, low paired rate, less erroneous vectors
VVH/2-PTV (Baek, S. J. and Lee, S. J. (1996) [12])	Low	2	2	Particles in the same search domain move approximately at the velocity	Fair tracking, many erroneous vectors

3.1. Category A: Basics of PIV and Post-Processing

In this section, we describe the basic studies on the PIV measurement for velocity fields, the improved algorithms of PIV/PTV, and the post-processing. Here two pioneering studies in PTV are introduced. One is a smooth trajectory of particles in four step frames introduced by Nishino, K., Kasagi, N. and Hirata, M. (1989) [11], and the other is a cross correlation method which estimates the similarity of particle distribution patterns between two frames introduced by Yamamoto, F., Wada, A., Iguchi, M. and Ishikawa, M. (1996) [7]. In Ref. [7], we showed that Equation (5) for the binary image method can be derived from an exact form of cross-correlation of Equation (1) for the brightness distribution method mathematically, by using a set theory and a step function from a general equation defined in an integral form. The characteristics of the two types of cross-correlation methods were discussed based on the derived expressions of cross-correlation. Furthermore, we proposed a new relation among the correlation parameters including the time interval, identification domain size, imaginary particle size, and the velocity gradient tensors in order to raise applicability of the cross-correlation method.

We would like to describe the motivation/reason why various PIV/PTV algorithms have been developed by many researchers; most of the conventional methods cannot obtain raw velocity data with high accuracy for the differential quantities such as acceleration, vorticity and velocity gradient tensor and also for the integral quantities such as streamline and pressure, and some post-processing techniques are required to modify the raw data, for instance to satisfy the continuity equation. Moreover, for shortening calculation time and eliminating the mismatched velocity vectors, many ideas have been proposed.

In the image correlation method, the particle displacement varies when the fluid velocity in the inspection region is non uniform due to the local rotation and/or strain rate of the fluid. As a result, the width of the correlation coefficient peak spreads, and the error of estimated velocity increases. Westerweel J. (2008) [13] examined the influences of the size and time interval of the particle image on the errors in the velocity distribution of fluid flow with shear strains. On the other hand, most PTV algorithms are not appropriate for calculating the velocity vectors of a fluid flow subjected to strong deformation, because these algorithms deal only with flows due to translation. Accordingly, it is necessary to develop an algorithm applicable to flows subjected to strong deformations such as rotation, shear, expansion, and compression. In Refs. [9] and [14], we proposed a novel particle tracking algorithm using a velocity gradient tensor (VGT) which deals with strong deformations and demonstrated that the algorithm is applicable to key fluid motions (rigidly rotating flow, Couette flow, and expansion flow) as shown in **Figure 1**. Furthermore, the performance of the algorithm was compared with the binary image cross-correlation method (BICC) [7], the four-consecutive-time-step particle tracking method (4-PTV) [11], and the spring model particle tracking algorithm (SPG) [10] using simulations and experimental

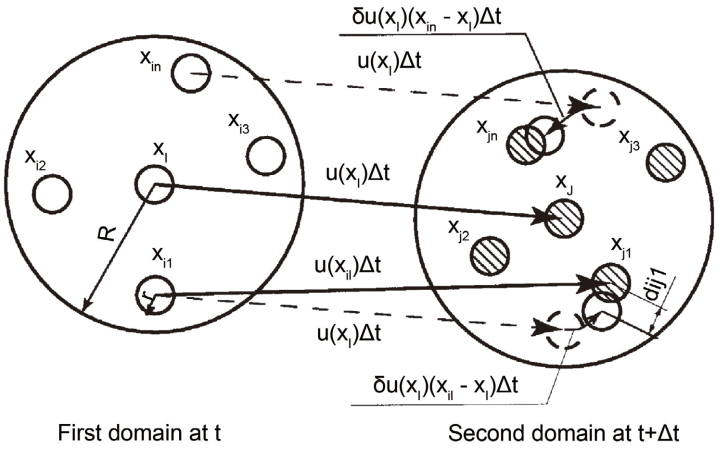

Figure 1. Overlapping condition of particles using the velocity gradient tensor [9].

data. As a result, the VGT algorithm was useful and applicable for the highly accurate measurement and analysis of fluid flows subjected to strong deformations as shown in **Figure 2**. We examined the applicability of the VGT method quantitatively for complicated flows, which included a wide dynamic range in wavenumber by simulations of Rankine vortex flows, Karman vortex-shedding flows around a rectangular cylinder and homogeneous turbulent flows, which were numerically solved by using the unsteady Navier-Stokes equations. The results showed that the VGT technique, using only two frames to estimate velocity, performed better than the four-frame PTV technique and had a remarkably higher tracking performance than those of typical conventional PTV algorithms as shown in **Figure 3** and **Figure 4**.

There is a PIV algorithm applying the image deformation corresponding to the strong velocity gradient tensor such as such as rotation, shear, expansion, and compression to interrogation window image. Scarano, F. (2001) [15] reviewed the iterative image deformation method. In Ref. [16] we developed a method called Direct Measurement of Vorticity (DMV in abbreviation) for digital particle images, unlike previous methods for calculating the vorticity from PIV/PTV velocity data. The idea of DMV is based on that the vorticity is determined directly from the average angular displacement of rotation between two matched patterns. In order to improve the stability and precision of the angular displacement, coordinate mappings from polar coordinates are used instead of Cartesian coordinates to depict gray level patterns. The results of a Monte Carlo simulation of an Oseen-vortex flow indicated that the accuracy of the DMV method is independent of the spatial resolution of the velocity sampling, and the errors in the velocity field do not propagate into the vorticity field unlike some finite difference methods do. We concluded that the DMV method can be used to extract the vorticity field from digital images.

We introduce a pioneering research of PIV analysis published by Okuno, T., Sugii, Y., and Nishio, S. (2000) [17] which dealt with direct measurement of spatial

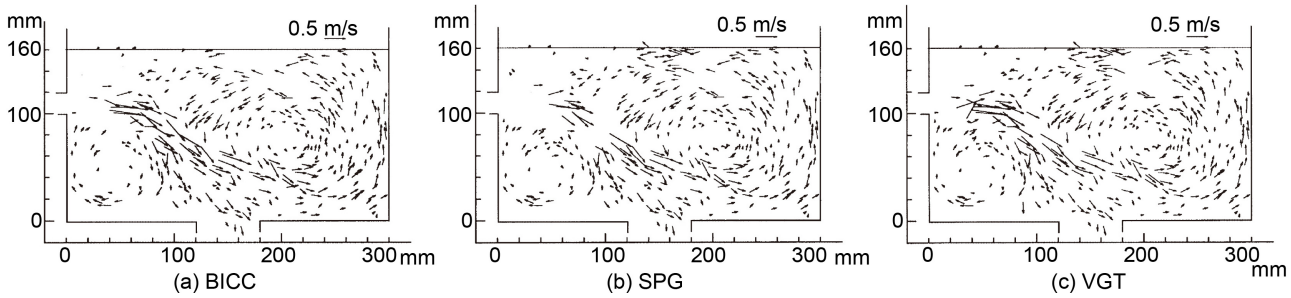

Figure 2. Velocity maps obtained from the three types of PTV. (a) BICC, (b) SPG, (c) VGT [9].

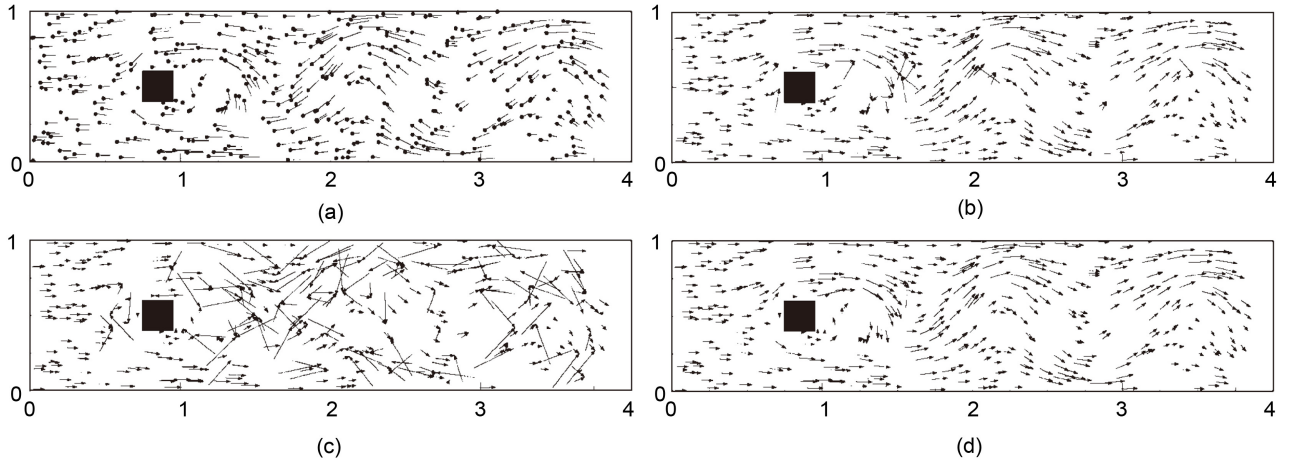

Figure 3. Validation using a Karman vortex-shedding flow (Re = 500): (a) the simulation image, (b) 4PTV, (c) BICC and (d) VGT [14].

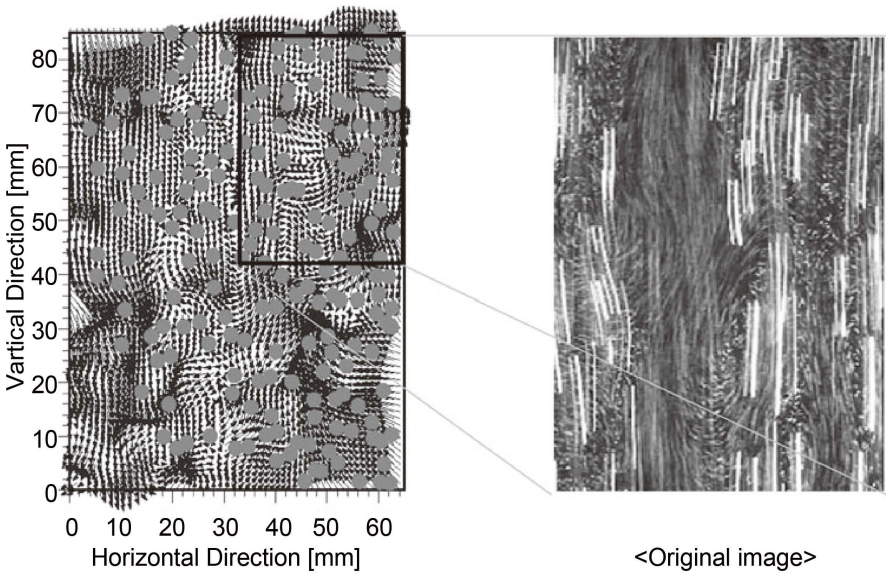

Figure 4. An example of an experimental application to bubbly flow [14].

derivatives included in the Navier-Stokes equation. Their technique enabled us to measure not only the velocity fields but also the pressure fields and satisfied the equation of continuity at the same time.

In Ref. [8] we proposed a new algorithm of Delaunay Tessellation PTV (DT-PTV in abbreviation) to track particles in images from a PTV system by making use of the Delaunay tessellation (DT) as shown in **Figure 5**. We calculated the balance of the inflow and outflow flow rates on the three sides of the DT triangle consisting of three points in the vicinity where the velocity vector is obtained. When the balance is achieved, the continuity equation is satisfied and the velocity vectors are regarded as correct; otherwise, the vectors are judged to be spurious and to be removed. As a result, the DT-PTV showed better performance of particle pair matching and that it was strong at measuring strain rate and vorticity of fluid flow.

In Ref. [18] we proposed a PIV technique based on fuzzy inference to determine whether the matched vectors are correct or spurious, and showed the flexibility with several factors in the application.

In general, vorticity distributions and stream functions are not accurately obtained by the conventional methods. Accurate post-processing methods are required in order to analyze the detailed flow structures from the scattered velocity data of PTV.

In Ref. [19] we proposed a new post-processing algorithm for rearrangement of a velocity map based on ellipsoidal differential equations (Laplace Equation Rearrangement (LER), Biquadratic Equation Rearrangement (BER) with the biquadratic order Laplace's equation); this method utilizes the velocity vectors obtained by PTV such as sampled vectors in **Figure 6** as discrete boundary conditions. The rearranged velocity vector was obtained by LER or BER. Furthermore,

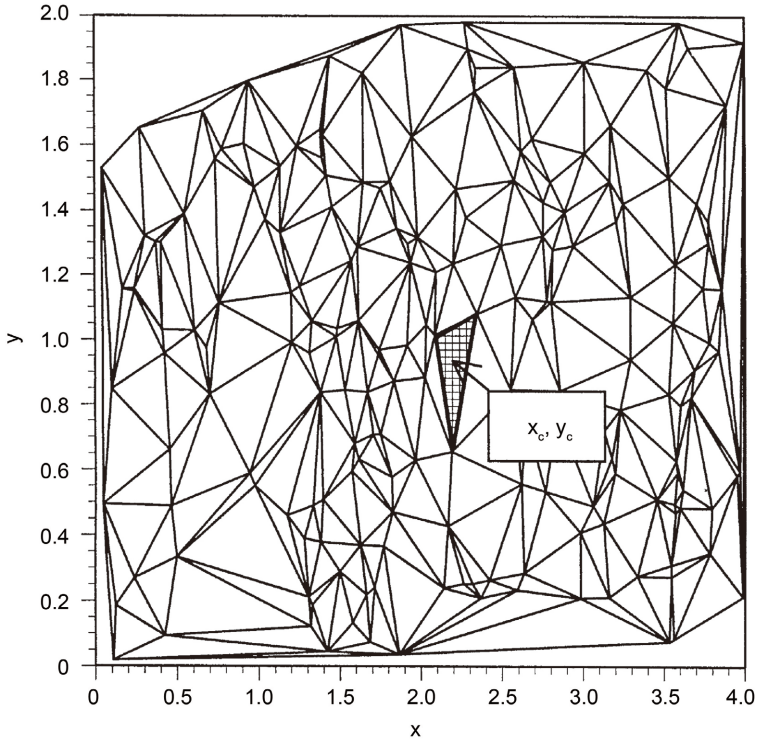

Figure 5. Selection of an arbitrary triangle with center in image A ($t = t_0$) [8].

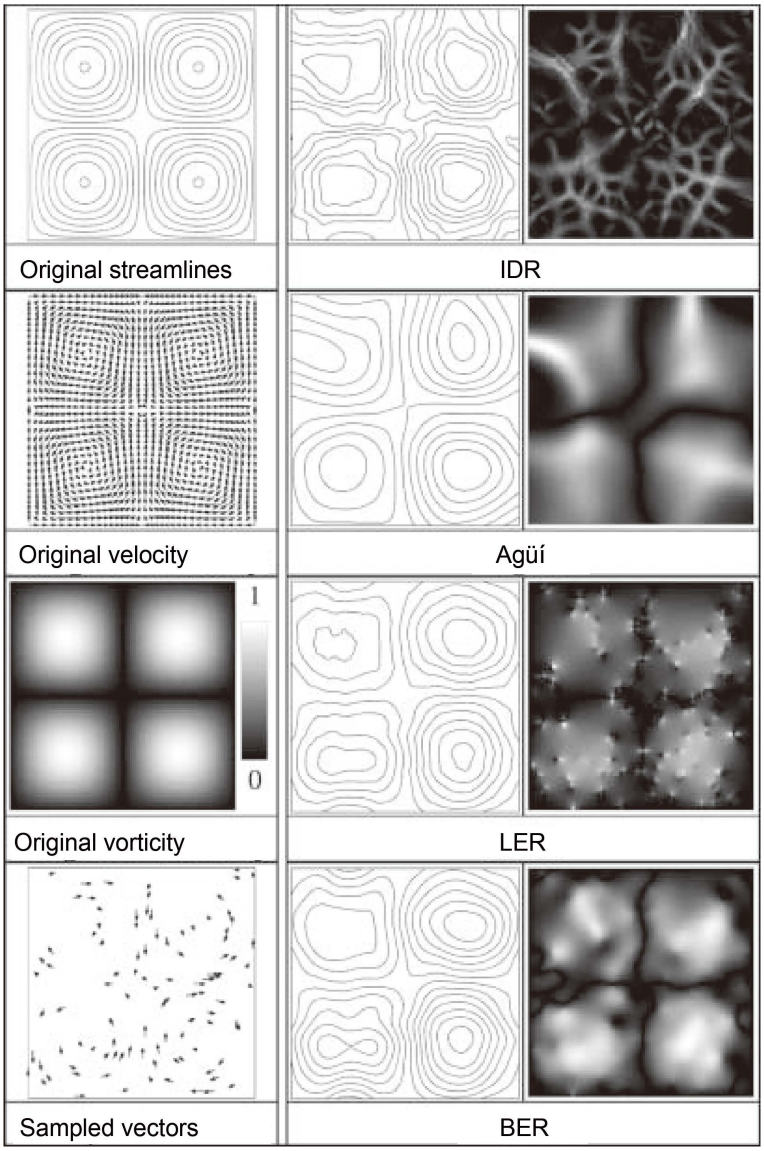

Figure 6. Results of application to vortex flow (IDR, Agüí's method [20], LER and BER [19]).

VCP (velocity correction potential) and IVCP (improved velocity correction potential) methods were proposed to fully satisfy the equation of continuity. The performance of their algorithms was examined by applying it to two-dimensional vortex flows and isotropic turbulent flows. **Figure 6** shows an example of the results. From this figure, the valid streamline with four circulation is obtained clearly by LER and BER. On the other hand, the vorticity distribution is not obtained correctly using LER and Inverse Distance Rearrangement (IDR) method. The vorticity distributions obtained by BER and Agüí's method [20] are a smooth and similar to the original. We concluded that BER had the highest accuracy among several conventional methods for detecting vorticity and streamlines.

Erkan, N., Ishikawa, M., and Okamoto, K. (2006) [21] applied a dynamic

(Time-Resolved) PIV to high-speed gas flow in a narrow channel with an obstacle. A high-speed camera and a Nd:YLF high repetition double-pulse laser were used. A large-scale structure of turbulence at the edge of the thin plate was clearly visualized in the temporal domain. The fluctuation velocities in the whole flow target area were simultaneously measured for high-speed turbulent flows. Ishikawa, M., Irabu, K., and Teruya, I. (2007) [22] applied POD (Proper orthogonal decomposition) to fluctuation vectors for a liquid phase including a complicated bubbly flow. The effect of POD is the spatio-temporal smooth filter by reconstruction of velocity using lower-order modes. Semeraro, O., Bellani, G. and Lundell, F. (2012) [23] showed that after extracting spatio-temporally fluctuating flow field modes, POD can be used to complement the velocities after removing the mismatched velocity vectors. The mismatched vectors have high-frequency components and high modes with low energy in POD. If the optimum frequency and mode are selected, the coherent structure of turbulence can be extracted without the influence of mismatched vectors by making use of POD.

Sciacchitano, A., Scarano, F. and Wieneke, B. (2012) [24] proposed a method that can measure local acceleration and convection acceleration by the PIV, using an image system with sufficient spatial resolution and a fast frame rate to capture spatio-temporal changes in velocity for three or more consecutive particle images. Lynch K. and Scarano F. (2013) [25] and Pröbsting, S., Scarano, F., Bernardini, M. and Pirozzoli, S. (2013) [26] developed a Time-Resolved PIV System and a Time-Resolved tomographic PIV System, respectively, with improved time resolution using a high-speed camera and a timing chart of LASER lighting. Schanz, D., Gesemann, S., and Schröder, A. (2016) [27] presented a Shake-The-Box as the new 3D-PTV. The method uses the IPR (Iterative Particle Reconstruction) method [28] to obtain 3D positions of particles with high accuracy. The particles that can move continuously for 4 or more frames are regarded as correct particles, and this operation is repeated at multiple frames to increase the acquisition rate of the correct trajectory. As a result, the generation of ghost particles is dramatically suppressed.

3.2. Category B: Simultaneous Measurement of Velocity and Temperature, and 3-D PIV

In this section, we introduce some researches on simultaneous measurement techniques for velocity vectors and temperature distribution as well as on 3-D PIV/PTV. For both techniques, new hardware systems with color information are required. The former utilizes the temperature-sensitive liquid crystals as tracing particles and a color CCD camera to record the images of the tracer particles illuminated by a sheet light, or a laser induced fluorescent (LIF) technique with a brightness intensifier. For the 3-D PIV/PTV two or more color CCD cameras and 3-D illumination system, there is another technique for 3-D PTV which utilizes a single color CMOS camera with rainbow color sheet illumination using a display projector.

Many papers on simultaneous measurement of velocity vectors and temperature distribution using temperature-sensitive liquid crystals and a color CCD camera had been published around 2000 or before. After that, Funatani, S., Fujisawa, N. and Ikeda, H. (2004) [29] and Someya, S., Okura, Y., Uchida, M. Sato, Y. and Okamoto, K. (2012) [30] published papers on a two-color LIF method and a phosphorescent lifetime method, respectively.

Papers on 3D-PIV have been increasing since 2000, because more experimental knowledge of 3D unsteady and turbulent flows is needed. However, the equipment adjustment of a 3D-PIV is complicated in terms of hardware, and also the equipment is expensive. For example, Atkinson C. and Soria J. (2009) [31], Scarano F. (2012) [32], Scarano F. and Poelma C. (2009) [33], Watamura, T., Tasaka, Y. and Murai, Y. (2013) [34], and de Silva, C. M., Baidya, R., and Marusic, I. (2012) [35] published papers on Tomographic 3D-PIV and other 3D techniques. Scarano F. *et al.* (2015) [36] developed a helium-filled soap bubble with the specific gravity close to unity and a diameter of less than 1 mm for tracers to better follow high-speed airflow in wind tunnels, and then applied large-scale tomographic PIV. Noto, D., Tasaka, Y. and Murai, Y. (2021) [37] proposed a seeding particle-based color-to-depth calibration methodology for 3D color PTV using a single camera and volumetric rainbow gradient illumination. The use of sheet-color illumination from a liquid crystal display projector enables in situ calibration; namely, the color-to-depth relationships of particles seeded in fluid are determined without inserting any calibration equipment or taking a different optical setup. The performance of the proposed method was evaluated using a rotating flow in a cylindrical tank by comparing its results with the flow fields measured by conventional PIV. They concluded as follows; good accordance in comparison with the highly 3D flow suggested the applicability of the present methodology for various flow configurations.

3.3. Category C: Application to Multiphase Turbulent Flows

Until the mid-1990s, velocity measurements in multiphase turbulent flows were made by LDVs and PDAs. However, since they are point measurement methods, it is not possible to measure the velocities of whole flow fields at the same time. In the latter half of the 1990s, the advantages of PIV were recognized and became widespread, and attempts to simultaneously measure the velocities of the whole flow field of fluid (liquid phase, gas phase) and solid phase began. In Ref. [2], Adiran, R.J. describes as the application of PIV to multiphase flow is viable and valuable. Since 2000, the number of papers applying PIV to multiphase turbulence has increased rapidly.

In Ref. [38] we investigated the inverse energy cascade which is one of the important phenomena to enhance the large-scale flow instability in bubbly flow, by measuring a local two-phase flow structure driven by buoyant bubbles using PTV with conditions as shown in **Table 2**. The flow field of the liquid phase was measured by separating an original image to respective phase images using a

Table 2. Experimental conditions [38].

Variable condition		CASE 1	CASE 2	CASE 3	CASE 4	CASE 5
Average void fraction	α [%]	0.333	0.612	0.855	0.913	1.062
Average bubble radius	R [mm]	0.60	0.64	0.78	0.86	0.89
Standard deviation of bubble radius	R' [mm]	0.11	0.15	0.25	0.28	0.28
Average rising velocity of bubble	V_{ave} [m/s]	0.100	0.109	0.117	0.146	0.157
Average bubble Reynolds number	Re [-]	12.0	14.0	18.3	25.1	28.0
Average bubble Weber number	We [-]	0.80	1.01	1.42	2.44	2.93

Fixed conditions: Liquid Density = 960 kg/m^3, Kinetic viscosity of liquid = 1.0×10^{-5} m^2/s, Gas Density = 1.21 kg/m^3, Environmental pressure = 101.3 kPa, Temperature 13.0 - 17.5 degree C, Test tank size 0.10 m × 0.10 m × 0.10 m, Number of bubble injection needles = 16 (min) – 361 (max), Internal diameter of the injection needles = 0.20 mm, liquid depth (without bubble) = 0.90 m.

statistical thresholding method with separating image parameters of bubbles and particles as shown in **Figure 7**. The results obtained in the case where the bubble Reynolds number and the average void fraction were less than 30% and 1.5%, respectively, confirmed the large energy decay with a slope index steeper than −5/3 in the log-log diagram of an energy spectrum in a high wavenumber region as shown in **Figure 8**. An important relationship between the energy spectrum and the bubble interval distance was also detected.

In Ref. [39] we dealt with flow visualization and image measurement of bubbly flows around various shapes of cylinders in a coaxial confined double rectangular chamber, which was constructed to provide a wide two-dimensional uniform bubble distribution upstream. As shown in **Figure 9**, the experiment clarified that a wide two-phase convection was induced around the obstacle, though such an effect was not observed in the single-phase flow around objects. The spatial scale of the two-phase convection depended sensitively on the shape of the obstacle. Regular, staggard, and random arrangements of cylinders were also investigated to find the interaction associated with the convection. The measurement results of the void fraction, bubble velocity and liquid phase flow, which were obtained by image processing including PTV, elucidated the detailed mechanism of generating the convection. Murai Y. *et al.* (2018) [40] explored the mode transition of the two-phase flow using PIV for the case of injection of bubbles into Taylor-Couette flow which created new flow modes which had not been observed in single-phase flow conditions. They found that bubble injection intensified the axial displacement of the wavy Taylor vortices in the toroidal array, and there was a smooth switching to a spiral array when the azimuthal

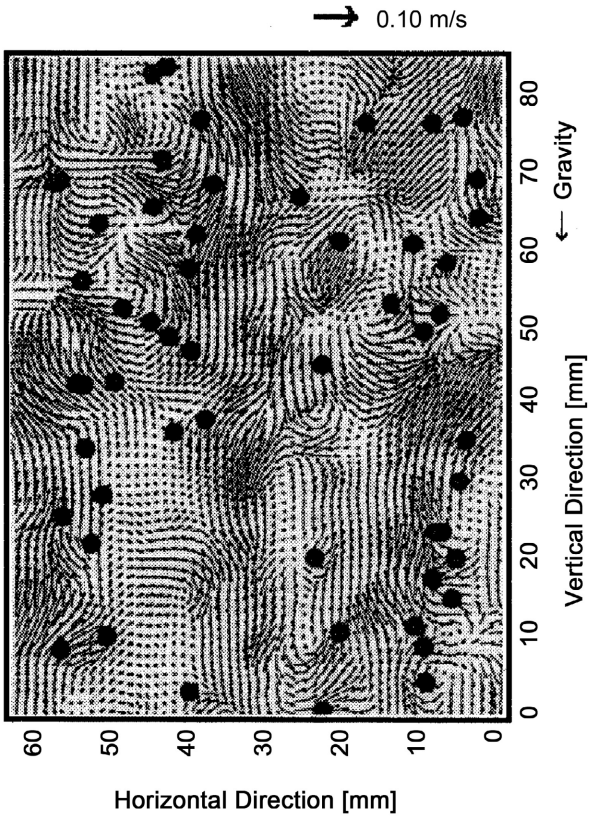

Figure 7. Two-phase flow structure measured by PIV (CASE 2) [38].

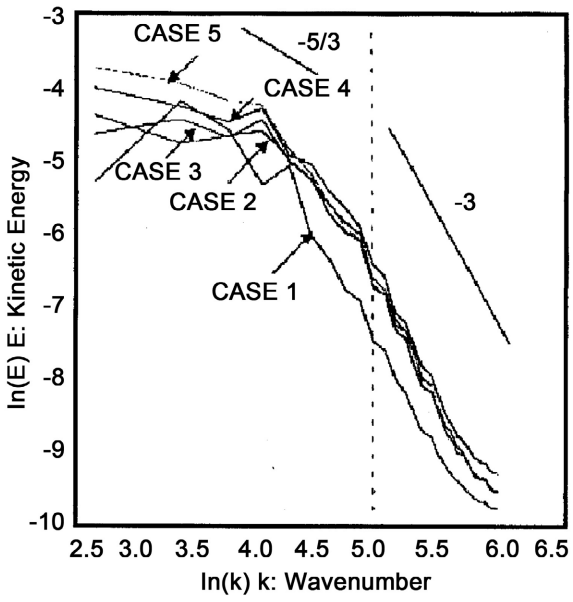

Figure 8. Measured energy spectra of liquid phase [38].

traveling velocities coincided between the two phases. During this vortical re-connection, the two counter-rotating vortices were attenuated asymmetrically. After the two phases interactively form a spiral array, the spiral-maintaining

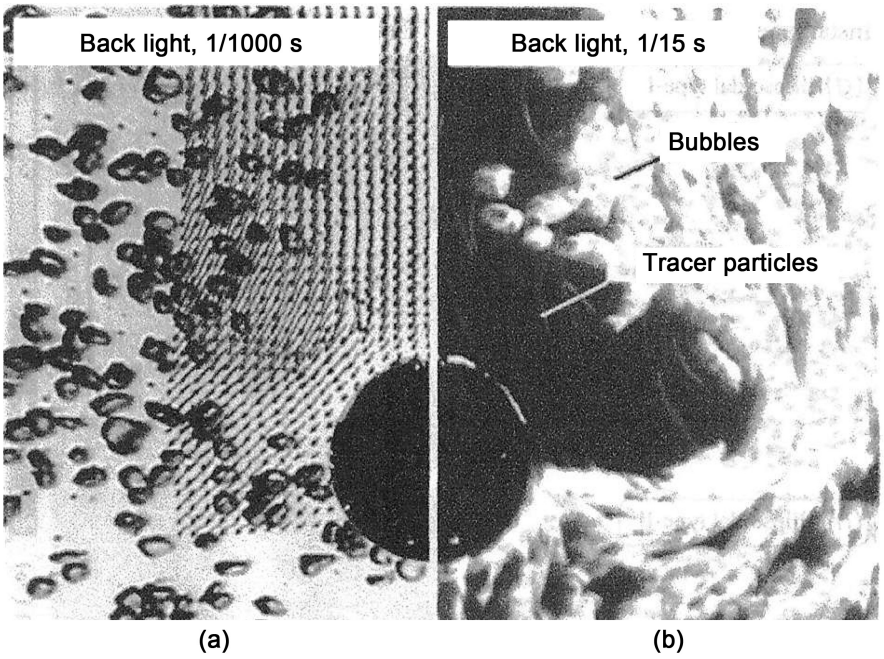

Figure 9. Local behavior of bubbles and tracers. (a) liquid velocity vectors obtained by PTV, (b) Pathline of bubbles and particles [39].

mechanism was weakened to restore toroidal vortices. These forward and backward mode transitions occurred periodically as the bubble injection flow rates increased. They concluded that modal switching was an evidence of two-way bubble-vortex interaction for an optimal state, causing the largest drag reduction reported in this regime.

In Ref. [41] we applied the PTV to a bubbly two-phase turbulent flow in a horizontal channel at Re = 2×10^4 to investigate the turbulent shear stress profile which had been altered by the presence of bubbles, and obtained streamwise and vertical velocity components of the liquid phase using a shallow depth-of-field (DOF) method under backlight photography. After bubbles and tracer particles were identified by binarizing the image, velocity of each phase and a void fraction were profiled in a downstream region. The result showed that the fluctuation correlation between the local void fraction and vertical liquid velocity provided a negative shear stress component which promoted frictional drag reduction in the bubbly two-phase layer as shown in **Figure 10**. The paper also dealt with the source of the negative shear stress considering bubble's relative motion to liquid. In fully-developed two-dimensional channel flow, there is no mean vertical velocity and no mean spanwise velocity, and the gradients of momentum in the streamwise and spanwise directions are negligible. In the case of bubbly flow, the turbulent shear stress consists of three terms as follows:

$$\tau_1 = -\rho\overline{(1-\alpha)}\overline{u'v'}, \tag{6}$$

$$\tau_2 = \rho\overline{\alpha'v'}\,\overline{u}, \tag{7}$$

$$\tau_3 = \rho\overline{\alpha'u'v'}, \tag{8}$$

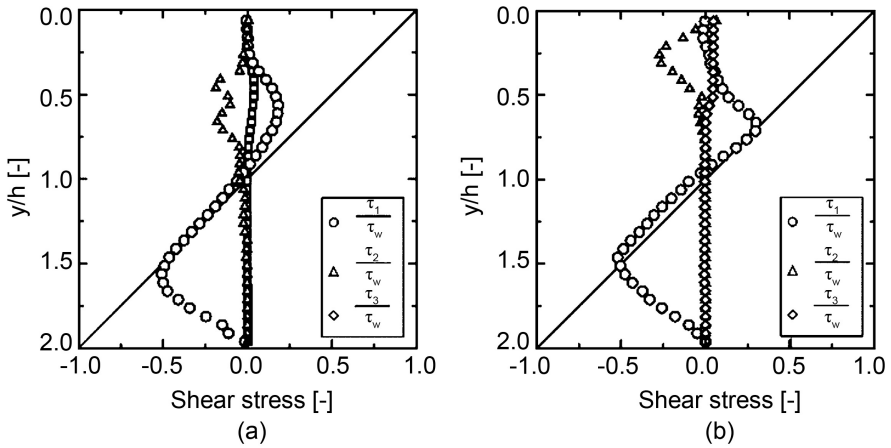

Figure 10. Turbulent shear stress profiles obtained by PTV data. a) x/h = 50, b) x/h = 800, where shear stresses τ_1, τ_2, and τ_3 are defined in Equations (6), (7) and (8), respectively, and τ_w means wall shear stress of the single-phase flow [41].

where α stands for the local void fraction. The stress component τ_1 is known as the Reynolds shear stress, whose absolute value is always reduced by mixing bubbles because of the factor $(1-\alpha)$. The stress components τ_2 and τ_3 are additional components as a two-phase correlation.

In Ref. [42] we investigated the effect of microbubble injection into a turbulent boundary layer, measuring the velocity fields of gas–liquid two-phase flow in a horizontal water channel using a PTV technique with an application of a lens system of the shallow focal depth-of-field (DOF) to a thin shear layer where the Reynolds shear stress is the highest. We were able to improve the spatial resolution of the PTV measurement results of the streamwise and spanwise velocity components and to visualize the motion of bubbles relative to the continuous phase in the near-wall region at three downstream positions, and discussed two-dimensional divergence of two-phase flow as shown in **Figure 11**. Considering the distribution of luminous flux, we first enhanced the illumination intensity to label the objects on images. With the assistance of an image processing filter, we then successfully improve the in-depth resolution of tracer particles and determine their positions more accurately. We showed that the averaged velocity right downstream of the bubble injector clearly decreased due to microbubbles. The local instantaneous flow structure around bubbles included no clear coherence because of highly turbulent background; however, the frequency spectrum analysis found that the bubbles reduced the kinetic energy in a frequency range higher than the bubble passing frequency.

In Ref. [43] we attempted to introduce a feedback loop of a bubble-injection approach to reduce skin–friction drag for ship in future applications. Hence, we established reduced-order models of unsteady bubbly flows from the information at the bottom of the ship with a limited number of sensors in practice, and developed a reconstruction technique that recovered instantaneous phase information of gas–liquid two-phase flows. The study introduced the so-called

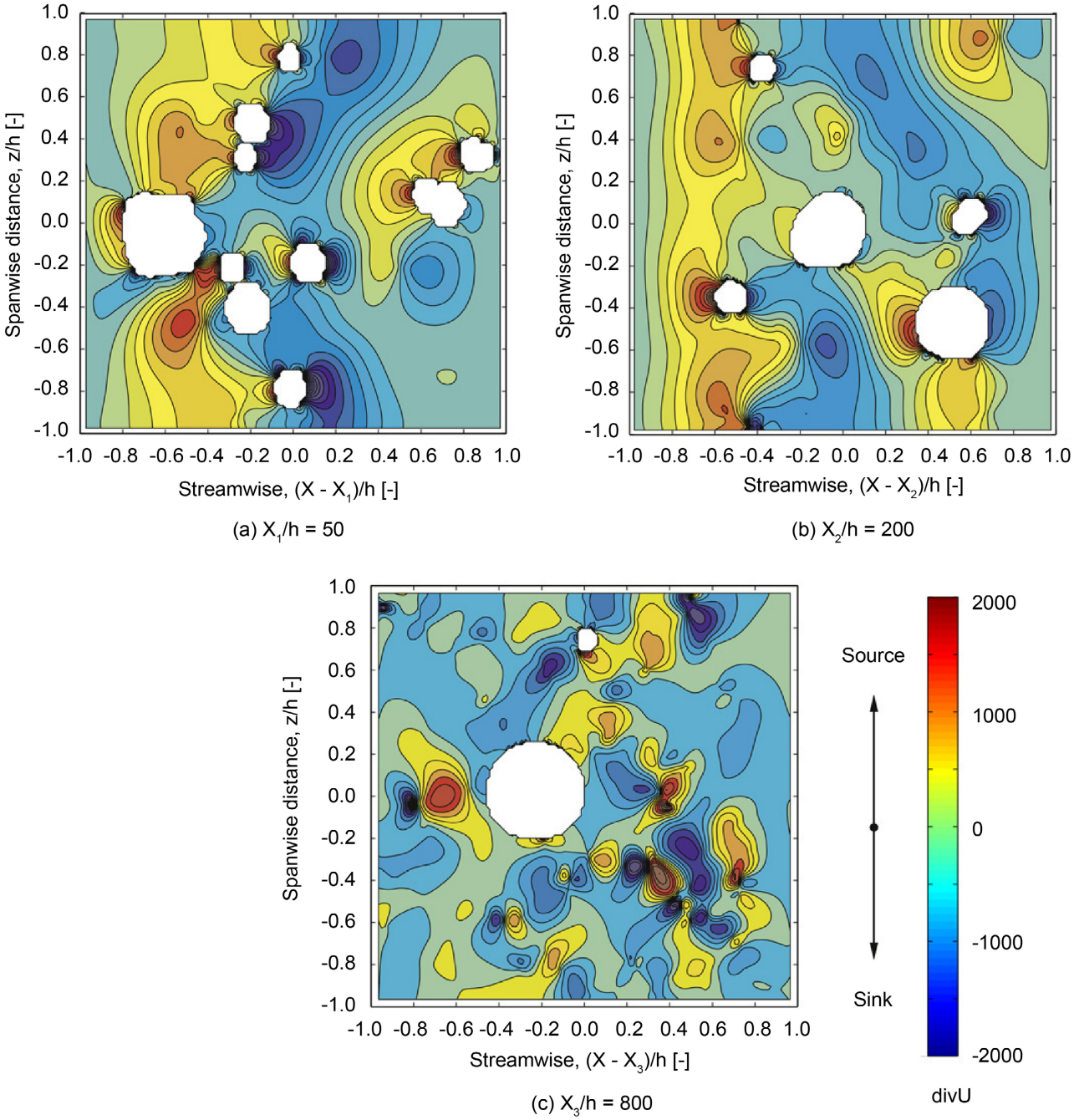

Figure 11. Two-dimensional divergence of two-phase flow at the three downstream positions (U = 2.0 m/s, α = 0.17%). Sources are drawn with reddish color, and sinks with bluish. White parts are bubbles. (a) X_1/h = 50; (b) X_2/h = 200; (c) X_3/h = 800 [42].

stochastic estimation and reconstructed bubble distribution based on electrical impedance. We simulated the flow at the bottom of a ship using a horizontal channel and installed a 16-channel electrode array on the upper wall to acquire time histories of electrical impedance. The relation between the bubble distribution and the electrical impedance was determined by simultaneous image measurement using a high-speed video camera. Once the coefficients of the linear relation between the electrical impedance and the local void fraction were calcu-

lated, two-dimensional bubble distribution can be estimated only from voltages at the 16 electrodes. The proposed technique was examined over a range of void fractions and flow velocities, and the capabilities of the stochastic estimation applied to bubbly flow reconstruction were demonstrated by comparing the reconstructed/predicted images with the original ones as shown in Figure 12.

In Ref. [44] we proposed an image analysis method for measuring bubble velocity fields at high bubble number density. It is based on computing the cross correlation of bubble images with multiple spatial resolutions, *i.e.*, a recursive cross correlation technique. By comparing several PTV and PIV schemes, it was confirmed that the recursive cross correlation led to the best measurement results because of the robustness with respect to optical and dynamic characteristics of bubbles. The method was applied successfully to the measurement of bubble motion in bubble plumes accompanying strong unsteadiness over a wide frequency range. The results revealed that high frequency fluctuations of bubble velocities grew in the shear layer and near the top surface, while low frequency fluctuations dominated in the middle part of the tank as shown in Figure 13. The characteristic frequency divided the frequency spectrum of the bubble fluctuation intensity into two regions: where turbulent behaviors exist and where macroscopic convection patterns exist in the bubble plumes.

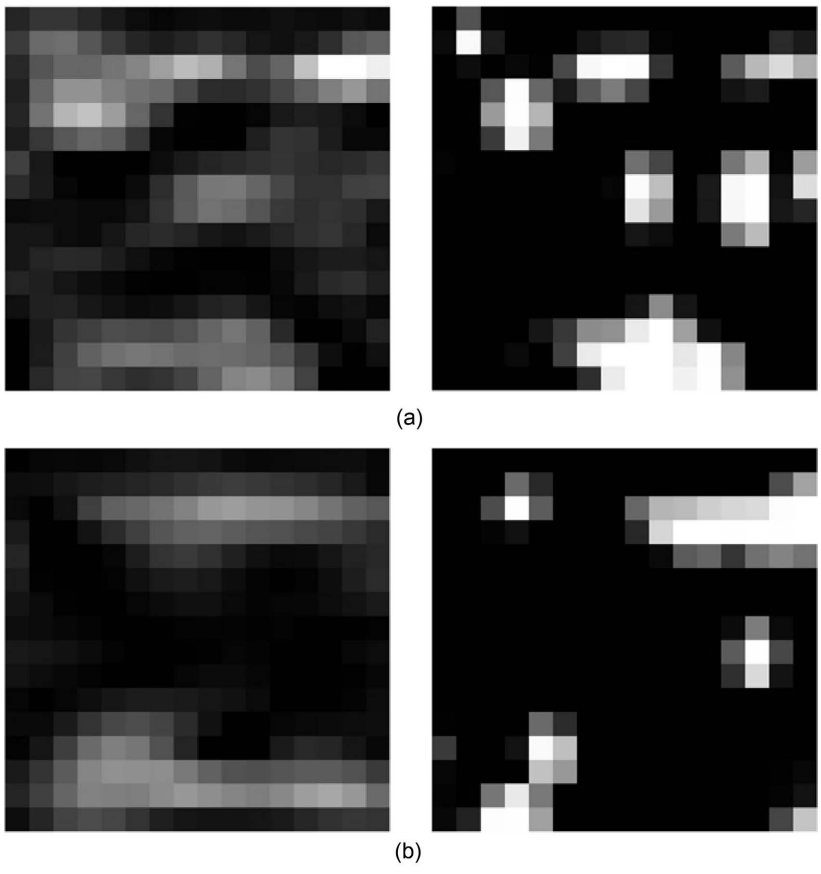

Figure 12. Comparison between the reconstructed images (left) and original ones (right) from case A: (a) high correlation frame; (b) low correlation frame [43].

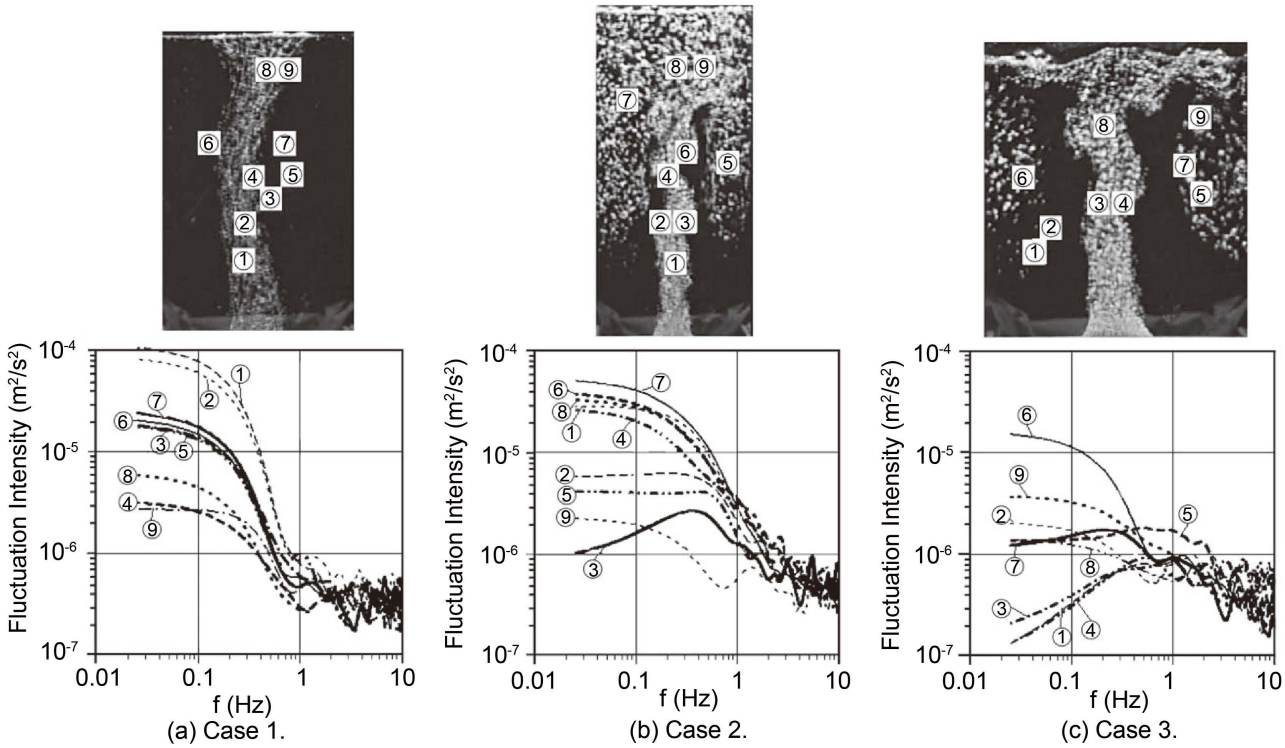

Figure 13. Frequency spectra of bubble fluctuation velocities, (a) Case 1: H(Water level)/W(Tank width) = 1.5 and low gas flow rate, (b) Case 2: W/H = 2 and high gas flow rate, and (c) Case 3: W/H = 1 and high gas flow rate [45].

According to translational equation of motion of a bubble, there is a method to obtain the liquid phase flow velocity by the inverse problem, which is obtained from the relative velocity with the bubble velocity by PTV. In Ref. [45] we proposed an algorithm for estimating liquid phase flow field from measurement data of bubble motion. A liquid velocity along the trajectory of the bubble is inversely calculated by equation of the translation motion of bubble. Whole field liquid flow structure is also estimated using spatial and/or temporal interpolation method. The applicability of the algorithm is examined with Taylor-Green vortex flow as an analytical test case, and with a bubbly plume as an experimental demonstration.

Ishikawa, M. (2017) [46] applied a PIV to a flow around a steel bridge beams. The equation of translational motion of the droplet was used. The gas phase velocity in the equation was used as the averaged velocity vector of the whole field obtained by PIV. The location where the corrosion by sea-water mist progresses rapidly was estimated.

3.4. Category D: Application to Fluid Machinery

It is extremely difficult to visualize the internal flow of a fluid machine with three-dimensional blades and take an image, but it has long been desired by industry. No other papers were found in the scope of our investigation before we published a study of PIV application to the internal flow of turbomachinery.

In Ref. [47] we applied PTV to the internal flows of a torque converter (T/C

acronym) widely used in automatic transmission cars. The internal flows of T/C were visualized by using a transparent apparatus made of acrylic resin, and visualized images were processed to determine velocity vectors using the binary image cross-correlation (BICC) method that is one of the PTV techniques. The velocity vectors were obtained at randomly distributed points in the flow field as shown in **Figure 14**.

In Ref. [48] we applied the PTV to measure flows around a Savonius type of wind turbine, and estimated the pressure field around the turbine, as well as evaluated the torque performance based on the measured velocity data in PTV. The measured velocity data were interpolated on a regular grid with a fourth-order ellipsoidal differential equation to generate velocity vectors satisfying the third-order spatio-temporal continuity both in time and space. Pressure fields by using the phase-averaged velocity vector information with respect to the turbine angle were obtained by three different types of pressure-estimating equations, *i.e.*, the Poisson equation, the Navier-Stokes equation and the sub-grid scale model of turbulence. As shown in **Figure 15**, it was found that a flow attached to the convex surface of the blades induced low-pressure regions to drive the turbine; namely, the lift force helped the turbine blades to rotate even when the drag force was insufficient. Secondary mechanisms of torque generation were also discussed.

3.5. Category E: Hybridization of PIV and CFD

Since Ma, X., Karniadakis, G. E., Park, H., and Gharib, M. (2003) [49] introduced the idea of flow simulation driven by digital PIV, the field of hybrid CFD combined with velocity measurement has been gradually growing. In Ref. [50] we introduced a new challenge of hybrid unsteady-flow simulation combining PTV and direct numerical simulation (DNS). Particle velocities on a laser-light sheet acquired with time-resolved PTV in a water tunnel were supplied to two-dimensional DNS with time intervals corresponding to the frame rate of the PTV. Hybrid velocity fields then approach those representing the PTV data in the course of time, and the reconstructed velocity fields satisfy the following

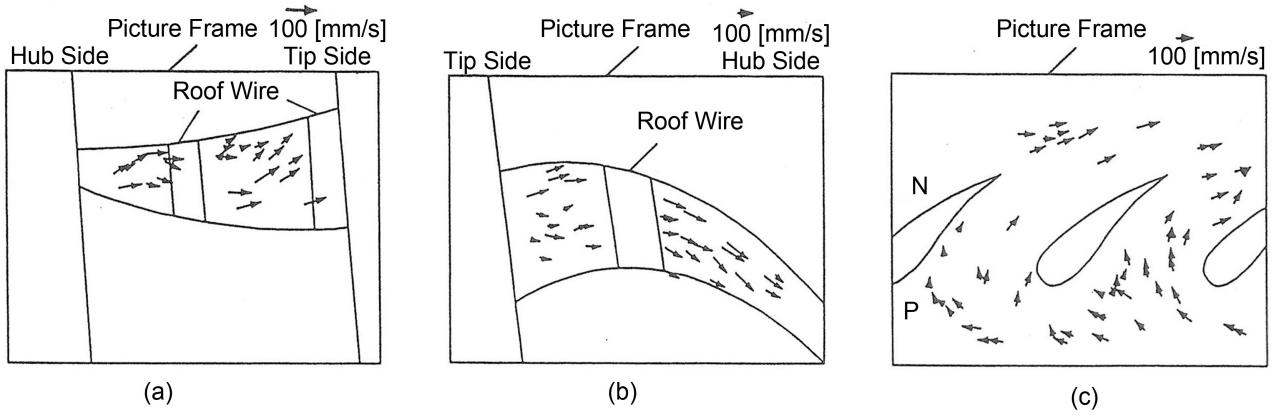

Figure 14. PTV measurement results; (a) Pump cascade flow, (b) turbine cascade flow, (c) Stator cascade flow [47].

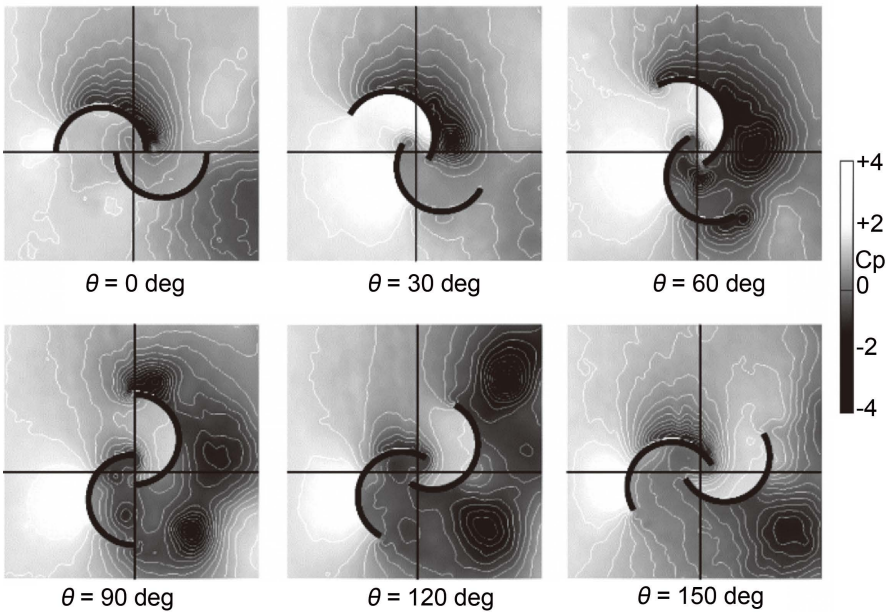

Figure 15. Pressure distribution for various angles of attack estimated by the Navier-Stokes equations at S (tip speed ratio) = 0.5 [48].

governing expression;

$$\begin{pmatrix} u \\ v \end{pmatrix}^{\text{Hybrid}} = \left[1-\varepsilon f(x,y)\right]\begin{pmatrix} u \\ v \end{pmatrix}^{\text{DNS}} + \varepsilon f(x,y)\begin{pmatrix} u \\ v \end{pmatrix}^{\text{PTV}}. \tag{9}$$

where $\varepsilon\left(0 \le \varepsilon \le 1\right)$ denotes the weight function on the PTV velocity field, and $f(x,y)\left(0 \le f \le 1\right)$ is called a patch function.

By extending the capabilities of the hybrid simulation to higher Reynolds numbers, we simulated flows past the NACA0012 airfoil over ranges of Reynolds numbers ($\mathrm{Re} \le 10^4$) and angles of attack ($-5^\circ \le \alpha \le -20^\circ$) and validated the proposed technique by comparing with experimental results in terms of the lift and drag coefficients. As shown in **Figure 16**, we also compared the results of turbulent energy with unsteady Reynolds-averaged Navier-Stokes (URANS) simulation in two-dimensions and showed the advantages of the hybrid simulation against two-dimensional URANS.

In Ref. [51] we developed a hybrid unsteady flow simulation technique combining direct numerical simulation (DNS) and PTV and demonstrated its capabilities by investigating flows past an airfoil. We rectified instantaneous PTV velocity fields in a least-squares sense so that they satisfied the equation of continuity, and fed to the DNS by equating the computational time step with the frame rate of the time-resolved PTV system as shown in **Figure 17**. As a result, we were able to reconstruct unsteady velocity fields that satisfied the governing equations based on experimental data, with the resolution comparable to numerical simulation. In addition, unsteady pressure distribution can be solved simultaneously. In the study, particle velocities were acquired on a laser-light sheet in a water tunnel, and unsteady flow fields were reconstructed with the

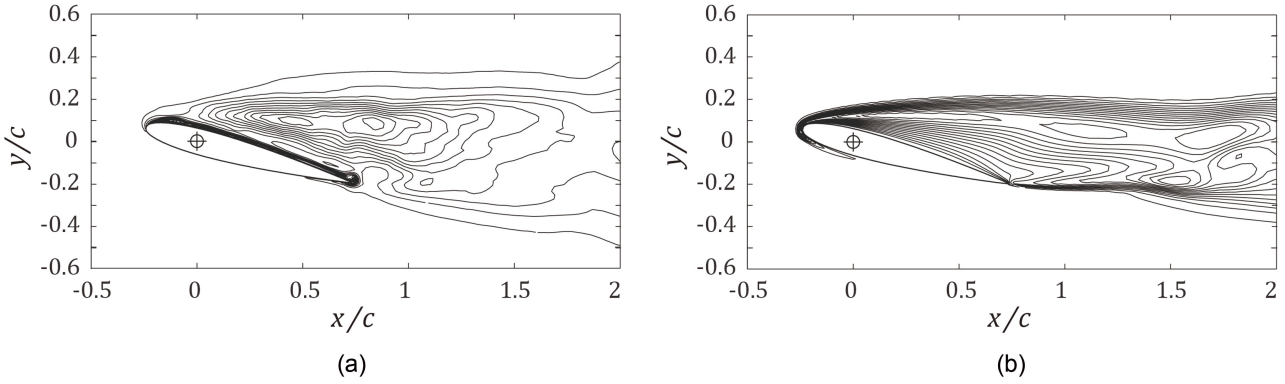

Figure 16. Comparison of the turbulent kinetic energy at Re = 10000 and $\alpha = 15^{\circ}$. (a) Hybrid simulation, (b) URANS including both resolved and modeled scales. Contour level: $0 \le \overline{u'^2 + v'^2} \big/ 2\left(+\bar{k}\right) \le 0.07u_{\infty}^2$ with an interval of $0.005u_{\infty}^2$ for both figures [50].

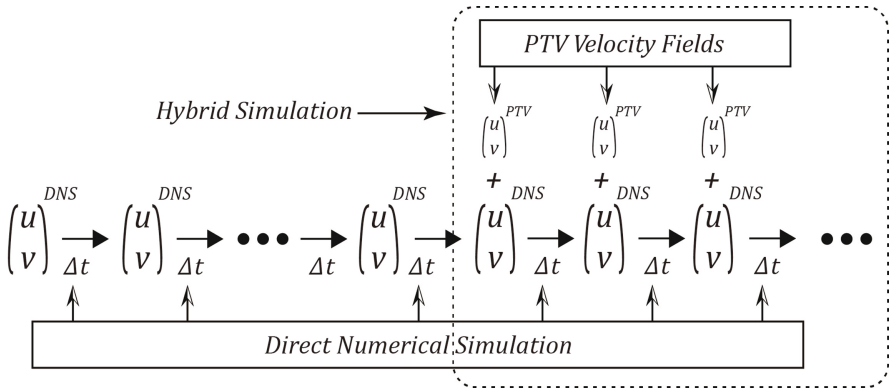

Figure 17. Conceptual diagram of the hybrid algorithm combining DNS and PTV [51].

hybrid algorithm solving the incompressible Navier-Stokes equations in two dimensions. By performing the hybrid simulation, we investigated nominally two-dimensional flows past the NACA0012 air-foil at low Reynolds numbers. We introduced the algorithm of the proposed technique and discussed the characteristics of hybrid velocity fields. In particular, we focused on a vortex shedding phenomenon under a deep stall condition ($\alpha = 15^{\circ}$) at Reynolds numbers of Re = 1000 and 1300, and compared the hybrid velocity fields with those computed with two-dimensional DNS as shown in **Figure 18**. In conclusion, we demonstrated that the hybrid simulation was capable of providing unsteady velocity field that was differentiable as well as pressure distribution that was smooth enough for quantitative analysis.

In Ref. [52] we extracted instability waves in a laminar planar jet using the hybrid unsteady flow simulation combining PTV and DNS. Unsteady velocity fields on a laser sheet in a water tunnel were measured with time-resolved PTV; subsequently, PTV velocity fields were rectified in a least squares sense so that the equation of continuity was satisfied, and were transplanted to a two-dimensional incompressible Navier-Stokes solver by setting a multiple of the computational time step equal to the frame rate of the PTV system. As shown in **Figure 19**, the unsteady hybrid velocity field approached that of the

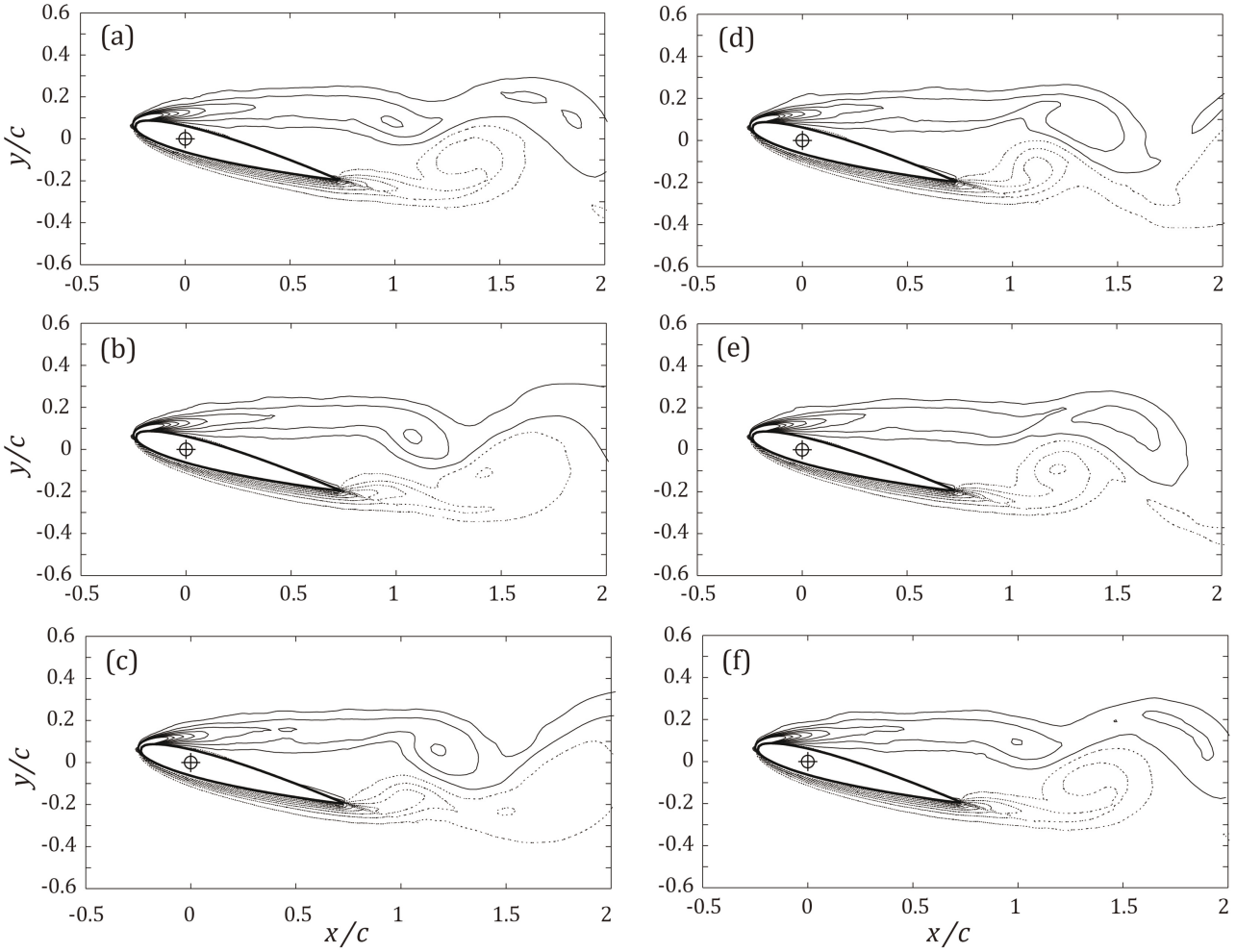

Figure 18. Time series of vorticity contours solved with the hybrid simulation at Re = 1300. One cycle of vortex shedding is displayed [51].

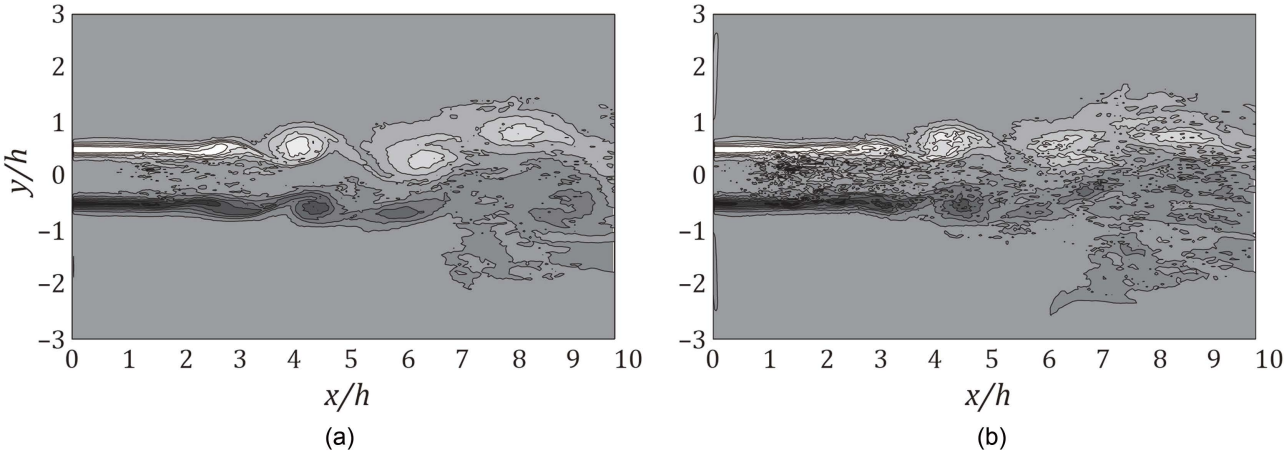

Figure 19. Comparison of vorticity contours from the hybrid simulation (Re = 4000), (a) $\varepsilon = 0.2\Delta t^{PTV}$, (b) $\varepsilon = 0.5\Delta t^{PTV}$ [52].

measured one over time, and we also simultaneously acquired the unsteady pressure field. The resultant set of flow quantities satisfied the governing equa-

tions, and the resolution was comparable to that of numerical simulation with the noise level much lower than the original PTV data. From hybrid unsteady velocity fields, we extracted eigenfunctions using bi-orthogonal decomposition as a spatial problem for viscous instability. We also investigated stability/convergence characteristics of the hybrid simulation referring to linear stability analysis.

Suzuki T. (2012) [53] developed another hybrid unsteady flow simulation technique combining PTV and DNS and demonstrated its capability at low Reynolds numbers. Applying an algorithm of this type of simulation generally becomes more challenging with increasing Reynolds number because the time interval of the frame rate for PIV becomes much greater than the required computational time step, and the PIV/PTV resolution tends to be lower than that necessary for computational fluid dynamics. To extend the applicability to noisy time-resolved PIV/PTV data, the proposed algorithm optimizes the data input temporally and spatially by introducing a reduced-order Kalman filter. The study established a framework of the Kalman-filtered hybrid simulation and proved the concept by tackling a planar jet flow at $Re \approx 2000$ as an example. He evaluated the filtering functions as well as convergence of the proposed algorithm by comparing with the existing PTV-DNS hybrid simulation, and showed some techniques available to hybrid velocity fields by analyzing vortical motion in the shear layers of the jet.

In Ref. [54] we have reviewed that data assimilation capabilities of hybrid type simulations integrating time-resolved PIV with unsteady CFD were characterized, and a series of algorithms developed previously were evaluated in terms of four criteria: 1) compatibility with the governing equations; 2) completeness of a set of flow quantities; 3) temporal and spatial filtering functions; and 4) spatial resolution. The study specifically introduced a hierarchy of three hybrid simulations combining time-resolved PTV and DNS from low to high fidelities: the proper orthogonal decomposition-Galerkin projection approach with proportional feedback of PTV data, the DNS solver with similar feedback, and the DNS solver with the extended Kalman filter. By solving a planar-jet problem at $Re \gg 2000$, we demonstrated that the resultant hybrid flow fields essentially a) satisfy the governing equations spatially and approximately temporally, and b) can provide instantaneous pressure fields c) with the noise levels substantially lower than those of the original PTV data and d) the resolution comparable to CFD. The results showed that increasing the feedback gain improved replicability, *i.e.*, the agreement between the simulation and the data; however, it degraded temporal compatibility and filtering functions. On the other hand, the fidelity enhances both replicability and spatial filtering, but increases computational cost.

4. Conclusions

The conclusion of this article is summarized as follows:

In the Introduction, many studies that played important roles as milestones in

the 1980s and 1990s respectively by Adrian R.J., and the research results from 2000 to recent were introduced in the books written by Adrian R. J., Westerweel, J., and Raffel, M. *et al.* In the present review article, avoiding duplication with their introduction, the articles that contributed to pioneering progress and development of the PIV studies were explained in five categories classified by our group.

Chapter 2 listed the basics and characteristics of conventional PIV and PTV, and briefly described their progress and development.

Chapter 3 introduced the research results for each Category.

In 3.1 Category A: In basics of PIV and post-processing, we showed the basic formula of the image correlation method, compared the conventional PIV with new PIV methods such as BICC, VGT, DT-PTV, and introduced the post-processing method. We introduced the studies proposing how to satisfy the equation of continuity, how to compute quantities in derivative forms such as a strain rate and a vorticity flow field, and integral quantities such as a streamline and a pressure field at high speed and with high accuracy.

In 3.2 Category B: In simultaneous measurement of velocity and temperature, and 3D-PIV, we introduced research papers on simultaneous measurement methods of temperature and velocity, and 3D-PIV, and stated that it was essential to improve the infrastructure of hardware systems such as tracer particles, lighting and optical systems, and color CCD cameras along with the development of the algorithm for image analysis.

In 3.3 Category C: In application to multiphase turbulent flows, we stated that in image measurement of multiphase flows it was first necessary to separate the recorded image into each phase. The research results which clarified energy spectra and the convection flow structure derived by bubble buoyancy in gas-liquid two-phase turbulent flows were introduced. These are the results of 2D-PTV and have not revealed a three-dimensional turbulent structure, but such 2-D studies may be useful for a qualitative understanding of gas-liquid two-phase turbulent flows.

In 3.4 Category D: In application to fluid machinery, we introduced the PTV measurement results of the internal flow of the torque converter made of transparent resin and those of the flow past the blades of the two-dimensional model of a Savonius type of wind turbine. It was shown that the distribution of the pressure, lift, drag and torque acting on the blades could be obtained after applying a post-processing technique to the measured velocity fields. Such achievements may contribute to improving the performance and design of fluid machinery.

In 3.5 Category E: In hybridization of PIV and CFD, we introduced a proposal for hybridization that uses PTV data as the velocity value in the Naver-Stokes equation and solves the N-S equation by the DNS method. The velocity field obtained by the hybridization satisfies the continuity equation. As a result of applying this method to analyze the flow around an NACA type of airfoil and a jet flow, it was made clear that the elucidation of the flow structure obtained by the

hybridization could be closer to the exact solution and lead to a deeper understanding of the flow phenomenon than only by experiment or CFD alone.

It is not easy for us to accurately predict the future development of PIV research and beyond the scope to collect all updated information. Because the areas where PIV is expected to be applied are expanding rapidly in space and time, as in the environment/energy and life sciences, and also hardware systems such as a camera, an optical system and an electronic information device are advancing very rapidly. However, as reviewing the research results in the five categories, we realize that there are still many basic issues to be explored. It may be stated that there is plenty room for development in PIV researches in the categories of the applications to multiphase turbulent flows and the hybridization of PIV and CFD.

Acknowledgements

We pay tribute to the researchers who have contributed to the research and development of PIV and PTV, the engineers and students who have been engaged in the experiments, and the authors of the reference papers cited in this article. We would like to express our sincere gratitude to the colleagues of our research group, especially Dr. Murai, Yuichi (Hokkaido University, Japan) and Dr. Suzuki, Takao (The Boeing Company, USA).

Conflicts of Interest

The authors declare no conflicts of interest regarding the publication of this paper.

References

[1] Adrian, R.J. (1991) Particle-Imaging Techniques for Experimental Fluid Mechanics. *Annual Review of Fluid Mechanics*, **23**, 261-304. https://doi.org/10.1146/annurev.fl.23.010191.001401

[2] Adrian, R.J. (2005) Twenty Years of Particle Image Velocimetry. *Experiments in Fluids*, **39**, 159-169. https://doi.org/10.1007/s00348-005-0991-7

[3] Adrian, R.J. and Westerweel, J. (2011) Particle Image Velocimetry. Cambridge University Press, Cambridge.

[4] Raffel, M., Willert, C.E., Scarano, F., Kähler, C.J., Wereley, S.T. and Kompenhans, J. (2018) Particle Image Velocimetry—A Practical Guide. 3rd Edition, Springer, New York. https://doi.org/10.1007/978-3-319-68852-7

[5] Gui, L.C. and Merzkirch, W. (1996) A Method of Tracking Ensembles of Particle Images. *Experiments in Fluids*, **21**, 465-468. https://doi.org/10.1007/BF00189049

[6] Kaga, A., Inoue, Y. and Yamaguchi, K. (1994) Pattern Tracking Algorithm for Airflow Measurement through Digital Image Processing of Visualized Images. *Journal of Visualization Society of Japan*, **14**, 108-115. (In Japanese) https://doi.org/10.3154/jvs.14.108

[7] Yamamoto, F., Wada, A., Iguchi, M. and Ishikawa, M. (1996) Discussion of the Cross-Correlation Methods for PIV. *Journal of Flow Visualization and Image Processing*, **3**, 65-78. https://doi.org/10.1615/JFlowVisImageProc.v3.i1.50

[8] Song, X., Yamamoto, F., Iguchi, M. and Murai, Y. (1999) A New Tracking Algorithm of PIV and Removal of Spurious Vectors Using Delaunay Tessellation. *Experiments in Fluids*, **26**, 371-380. https://doi.org/10.1007/s003480050300

[9] Ishikawa, M., Murai, Y., Wada, A., Iguchi, M., Okamoto, K. and Yamamoto, F. (2000) A Novel Algorithm for Particle Tracking Velocimetry Using the Velocity Gradient Tensor. *Experiments in Fluids*, **29**, 519-531. https://doi.org/10.1007/s003480000120

[10] Okamoto, K., Hassan, Y.A. and Schmidl, W.D. (1995) New Tracking Algorithm for Particle Image Velocimetry. *Experiments in Fluids*, **19**, 342-347. https://doi.org/10.1007/BF00203419

[11] Nishino, K., Kasagi, N. and Hirata, M., (1989) Three-Dimensional Particle Tracking Velocimetry Based on Automated Digital Image Processing. *Journal of Fluids Engineering*, **111**, 384-391. https://doi.org/10.1115/1.3243657

[12] Baek, S.J. and Lee, S.J. (1996) A New Two-Frame Particle Tracking Algorithm Using Match Probability. *Experiments in Fluids*, **22**, 23-32. https://doi.org/10.1007/BF01893303

[13] Westerweel, J. (2008) On Velocity Gradients in PIV Interrogation. *Experiments in Fluids*, **44**, 831-842. https://doi.org/10.1007/s00348-007-0439-3

[14] Ishikawa, M., Murai, Y. and Yamamoto, F. (2000) Numerical Validation of Velocity Gradient Tensor Particle Tracking Velocimetry for Highly Deformed Flow Fields. *Measurement Science and Technology*, **11**, 677-684. https://doi.org/10.1088/0957-0233/11/6/310

[15] Scarano, F. (2001) Iterative Image Deformation Methods in PIV. *Measurement Science and Technology*, **13**, R1-R19. https://doi.org/10.1088/0957-0233/13/1/201

[16] Ruan, X., Song, X. and Yamamoto, F. (2001) Direct Measurement of the Vorticity Field in Digital Particle Images. *Experiments in Fluids*, **30**, 696-704. https://doi.org/10.1007/s003480000249

[17] Okuno, T., Sugii, Y. and Nishio, S. (2000) Image Measurement of Flow Field Using Physics-Based Dynamic Model. *Measurement Science and Technology*, **11**, Article No. 667. https://doi.org/10.1088/0957-0233/11/6/309

[18] Shen, L., Song, X., Murai, Y., Iguchi, M. and Yamamoto, F. (2001) Velocity and Size Measurement of Falling Particles with Fuzzy PTV. *Flow Measurement and Instrumentation*, **12**, 191-199. https://doi.org/10.1016/S0955-5986(01)00016-4

[19] Ido, T., Murai, Y. and Yamamoto, F. (2002) Postprocessing Algorithm for Particle-Tracking Velocimetry Based on Ellipsoidal Equations. *Experiments in Fluids*, **32**, 326-336. https://doi.org/10.1007/s003480100361

[20] Agüí, J.C. and Jiménez, J. (1987) On the Performance of Particle Tracking. *Journal of Fluid Mechanics*, **185**, 447-468. https://doi.org/10.1017/S0022112087003252

[21] Erkan, N., Ishikawa, M. and Okamoto, K. (2006) Fluctuation Transfer Velocity Measurement in a Boundary Layer around a Thin Edge Plate Using Dynamic PIV. *Measurement Science and Technology*, **17**, Article No. 1350. https://doi.org/10.1088/0957-0233/17/6/010

[22] Ishikawa, M., Irabu, K. and Teruya, I. (2007) Time-Serial Analysis on Gas-Liquid Two-Phase Bubbly Flow Using POD. *AIP Conference Proceedings*, **914**, 361-366. https://doi.org/10.1063/1.2747454

[23] Semeraro, O., Bellani, G. and Lundell, F. (2012) Analysis of Time-Resolved PIV Measurements of a Confined Turbulent Jet Using POD and Koopman Modes. *Experiments in Fluids*, **53**, 1203-1220. https://doi.org/10.1007/s00348-012-1354-9

[24] Sciacchitano, A., Scarano, F. and Wieneke, B. (2012) Multi-Frame Pyramid Correlation for Time-Resolved PIV. *Experiments in Fluids*, **53**, 1087-1105. https://doi.org/10.1007/s00348-012-1345-x

[25] Lynch, K. and Scarano, F. (2013) A High-Order Time-Accurate Interrogation Method for Time-Resolved PIV. *Measurement Science and Technology*, **24**, Article ID: 035305. https://doi.org/10.1088/0957-0233/24/3/035305

[26] Pröbsting, S., Scarano, F., Bernardini, M. and Pirozzoli, S. (2013) On the Estimation of Wall Pressure Coherence Using Time-Resolved Tomographic PIV. *Experiments in Fluids*, **54**, Article No. 1567. https://doi.org/10.1007/s00348-013-1567-6

[27] Schanz, D., Gesemann, S. and Schröder, A. (2016) Shake-The-Box: Lagrangian Particle Tracking at High Particle Image Densities. *Experiments in Fluids*, **57**, Article No. 70. https://doi.org/10.1007/s00348-016-2157-1

[28] Wieneke, B. (2012) Iterative Reconstruction of Volumetric Particle Distribution. *Measurement Science and Technology*, **24**, Article ID: 024008. https://doi.org/10.1088/0957-0233/24/2/024008

[29] Funatani, S., Fujisawa, N. and Ikeda, H. (2004) Simultaneous Measurement of Temperature and Velocity Using Two-Colour LIF Combined with PIV with a Colour CCD Camera and Its Application to the Turbulent Buoyant Plume. *Measurement Science and Technology*, **15**, 983-990. https://doi.org/10.1088/0957-0233/15/5/030

[30] Someya, S., Okura, Y., Uchida, M., Sato, Y. and Okamoto, K. (2012) Combined Velocity and Temperature Imaging of Gas Flow in an Engine Cylinder. *Optics Letters*, **37**, 4964-4966. https://doi.org/10.1364/OL.37.004964

[31] Atkinson, C. and Soria, J. (2009) An Efficient Simultaneous Reconstruction Technique for Tomographic Particle Image Velocimetry. *Experiments in Fluids*, **47**, 553-568. https://doi.org/10.1007/s00348-009-0728-0

[32] Scarano, F. (2012) Tomographic PIV: Principles and Practice. *Measurement Science and Technology*, **24**, Article ID: 012001. https://doi.org/10.1088/0957-0233/24/1/012001

[33] Scarano, F. and Poelma, C. (2009) Three-Dimensional Vorticity Patterns of Cylinder Wakes. *Experiments in Fluids*, **47**, 69-83. https://doi.org/10.1007/s00348-009-0629-2

[34] Watamura, T., Tasaka, Y. and Murai, Y. (2013) LCD-Projector-Based 3D Color PTV. *Experimental Thermal and Fluid Science*, **47**, 68-80. https://doi.org/10.1016/j.expthermflusci.2012.12.019

[35] de Silva, C.M., Baidya, R. and Marusic, I. (2012) Enhancing Tomo-PIV Reconstruction Quality by Reducing Ghost Particles. *Measurement Science and Technology*, **24**, Article ID: 024010. https://doi.org/10.1088/0957-0233/24/2/024010

[36] Scarano, F., Ghaemi, S., Caridi, G.C.A., Bosbach, J., Dierksheide, U. and Sciacchitano, A. (2015) On the Use of Helium-Filled Soap Bubbles for Large-Scale Tomographic PIV in Wind Tunnel Experiments. *Experiments in Fluids*, **56**, Article No. 42. https://doi.org/10.1007/s00348-015-1909-7

[37] Noto, D., Tasaka, Y. and Murai, Y. (2021) In Situ Color-to-Depth Calibration: Toward Practical Three-Dimensional Color Particle Tracking Velocimetry. *Experiments in Fluids*, **62**, Article No. 131. https://doi.org/10.1007/s00348-021-03220-9

[38] Murai, Y., Song, X.Q., Takagi, T., Ishikawa, M., Yamamoto, F. and Ohta, J. (2000) Inverse Energy Cascade Structure of Turbulence in a Bubbly Flow: PIV Measurement and Results. *JSME International Journal Series B Fluids and Thermal Engineering*, **43**, 188-196. https://doi.org/10.1299/jsmeb.43.188

[39] Murai, Y., Sasaki, T., Ishikawa, M.A. and Yamamoto, F. (2005) Bubble-Driven Convection around Cylinders Confined in a Channel. *Journal of Fluids Engineering*, **127**, 117-123. https://doi.org/10.1115/1.1852478

[40] Murai, Y., Tasaka, Y., Oishi, Y. and Takeda, Y. (2018) Modal Switching of Bubbly Taylor-Couette Flow Investigated by Particle Tracking Velocimetry. *Experiments in Fluids*, **59**, Article No. 164. https://doi.org/10.1007/s00348-018-2620-2

[41] Murai, Y., Oishi, Y., Takeda, Y. and Yamamoto, F. (2006) Turbulent Shear Stress Profiles in a Bubbly Channel Flow Assessed by Particle Tracking Velocimetry. *Experiments in Fluids*, **41**, 343-352. https://doi.org/10.1007/s00348-006-0142-9

[42] Huang, J., Murai, Y. and Yamamoto, F. (2008) Shallow DOF-Based Particle Tracking Velocimetry Applied to Horizontal Bubbly Wall Turbulence. *Flow Measurement and Instrumentation*, **19**, 93-105. https://doi.org/10.1016/j.flowmeasinst.2007.10.003

[43] Zhou, W., Suzuki, T., Nishiumi, T. and Yamamoto, F. (2008) Reconstruction of Gas-Liquid Flows Using the Stochastic Estimation with a 16-Channel Electrode Array. *Measurement Science and Technology*, **19**, Article ID: 105402. https://doi.org/10.1088/0957-0233/19/10/105402

[44] Cheng, W., Murai, Y., Sasaki, T. and Yamamoto, F. (2005) Bubble Velocity Measurement with a Recursive Cross Correlation PIV Technique. *Flow Measurement and Instrumentation*, **16**, 35-46. https://doi.org/10.1016/j.flowmeasinst.2004.08.002

[45] Cheng, W., Murai, Y., Ishikawa, M, and Yamamoto, F. (2003) An Algorithm for Estimating Liquid Flow Field from PTV Measurement Data of Bubble Motion. *Transaction Visualization Society of Japan*, **23**, 107-114. https://doi.org/10.3154/tvsj.23.107

[46] Ishikawa, M. (2017) A Study on Flow Structure around a Bridge Beam and Behavior of Sea Water Mist. *Open Journal of Fluid Dynamics*, **7**, 340-347. https://doi.org/10.4236/ojfd.2017.73022

[47] Yamamoto, F., Wada, A., Iguchi, M. and Ishikawa, M. (1996) Discussion of the Cross-Correlation Methods for PIV. *Journal of Flow Visualization and Image Processing*, **3**, 65-78. https://doi.org/10.1615/JFlowVisImageProc.v3.i1.50

[48] Murai, Y., Nakada, T., Suzuki, T. and Yamamoto, F. (2007) Particle Tracking Velocimetry Applied to Estimate the Pressure Field around a Savonius Turbine. *Measurement Science and Technology*, **18**, Article No. 2491. https://doi.org/10.1088/0957-0233/18/8/026

[49] Ma, X., Karniadakis, G.E., Park, H. and Gharib, M. (2003) DPIV-Driven Flow Simulation: A New Computational Paradigm. *Proceedings of the Royal Society A*: *Mathematical, Physical and Engineering Sciences*, **459**, 547-565. https://doi.org/10.1098/rspa.2002.0981

[50] Suzuki, T., Sanse, A., Mizushima, T. and Yamamoto, F. (2009) Unsteady PTV Velocity Field Past an Airfoil Solved with DNS: Part 2. Validation and Application at Reynolds Numbers Up to $Re \leq 10^4$. *Experiments in Fluids*, **47**, 977-994. https://doi.org/10.1007/s00348-009-0692-8

[51] Suzuki, T., Ji, H. and Yamamoto, F. (2009) Unsteady PTV Velocity Field Past an Airfoil Solved with DNS: Part 1. Algorithm of Hybrid Simulation and Hybrid Velocity Field at $Re \approx 10^3$. *Experiments in Fluids*, **47**, 957-976. https://doi.org/10.1007/s00348-009-0691-9

[52] Suzuki, T., Ji, H. and Yamamoto, F. (2010) Instability Waves in a Low-Reynolds-Number Planar Jet Investigated with Hybrid Simulation Combining Particle Tracking Velocimetry and Direct Numerical Simulation. *Journal of Fluid Mechanics*, **655**,

344-379. https://doi.org/10.1017/S0022112010000893

[53] Suzuki, T. (2012) Reduced-Order Kalman-Filtered Hybrid Simulation Combining Particle Tracking Velocimetry and Direct Numerical Simulation. *Journal of Fluid Mechanics*, **709**, 249-288. https://doi.org/10.1017/jfm.2012.334

[54] Suzuki, T. and Yamamoto, F. (2015) Hierarchy of Hybrid Unsteady-Flow Simulations Integrating Time-Resolved PTV with DNS and Their Data-Assimilation Capabilities. *Fluid Dynamics Research*, **47**, Article ID: 051407. https://doi.org/10.1088/0169-5983/47/5/051407

Nomenclature

[Chapter 2]

$C_{1,fg}$: Cross-correlation coefficient between functions f and g for Equation (1)

$C_{2,fg}$: Cross-correlation coefficient between functions f and g for Equation (2)

$C_{5,fg}$: Cross-correlation coefficient between functions f and g for Equation (5)

D_{fg}: Quadratic difference between functions f and g

$\vec{D}_{PO}$: Displacement between the particle centers P and Q [m]

E_{fg}: Absolute difference between functions f and g

f: Function of brightness value for the first image

$\overline{f}$: Mean value of function f

g: Function of brightness value for the second image

$\overline{g}$: Mean value of function g

L: Summation of logical products of the binarized image in overlapped interrogation window

M: Image height

m: Number of the bright pixels in the first image

N: Image width

n: Number of the bright pixels in the second image

$\vec{v}$: Velocity vector [m/s]

Δt: Time interval [s]

Subscript

P: Particle center in the first image

Q: Particle center in the second image

[Section 3.1]

d: Distance between the two particle centers in shifted second image [m]

du: Velocity gradient tensor [s^{-1}]

R: Radius of the neighboring domain [m]

t: Time [s]

u: Velocity vector [m/s]

x: Particle center [m]

x_c, y_c: Coordinate of Center of Delaunay triangle in the DT-PTV

Δt: Time interval [s]

Subscript

I: A reference particle for the first image

i: Neighboring particles of the reference particle

J: A candidate particle for the second image

j: Neighboring particles of the candidate particle

[Section 3.3]

H: Water level or height in measured area [m]

R: Average bubble radius [mm]

R': Standard deviation of bubble radius [mm]

Re: Average bubble Reynolds number

U: Average velocity for the liquid phase [m/s]

V_{ave}: Average rising velocity of bubble [m/s]
W: Width in measured area [m]
We: Average bubble Weber number
α : Local void fraction or Average void fraction
ρ : Density [kg/m^3]
τ_1 : Reynolds shear stress [Pa]
τ_2 , τ_3 : Additional stress components as a two-phase correlation [Pa]
τ_w : Wall shear stress of the single-phase flow [Pa]

[Section 3.4]

C_p: Pressure coefficient
S: Ratio of peripheral tip speed to incident speed
θ Attack angle

[Section 3.5]

$f(x, y)$: Patch function for hybrid system
k: Turbulent kinetic energy [m^2/s^2]
Re: Reynolds numbers
u, v: Velocity component [m/s]
u', v' : Fluctuation velocity component [m/s]
u_∞ : Average velocity in experimental condition [m/s]
α : Attack angle
ε : Weight function on the PTV velocity fields